



OPEN ACCESS

RECEIVED
23 December 2020REVISED
24 March 2021ACCEPTED FOR PUBLICATION
19 April 2021PUBLISHED
26 May 2021

Original Content from
this work may be used
under the terms of the
[Creative Commons
Attribution 4.0 licence](#).

Any further distribution
of this work must
maintain attribution to
the author(s) and the title
of the work, journal
citation and DOI.



PAPER

A physical origin of cross-polarization and higher-order modes in two-dimensional (2D) grating couplers and the related device performance limitations

Galina Georgieva^{1,*} , Karsten Voigt^{1,2}, Pascal M Seiler^{1,2}, Christian Mai², Klaus Petermann¹
and Lars Zimmermann^{1,2}

¹ Technische Universität Berlin, Office HFT4, Einsteinufer 25, 10587 Berlin, Germany

² IHP—Leibnitz Institut für innovative Mikroelektronik, Im Technologiepark 25, 15236 Frankfurt (Oder), Germany

* Author to whom any correspondence should be addressed.

E-mail: galina.georgieva@tu-berlin.de

Keywords: two-dimensional (2D) grating couplers, silicon photonics, scattering, higher-order modes, cross-polarization, polarization splitting

Abstract

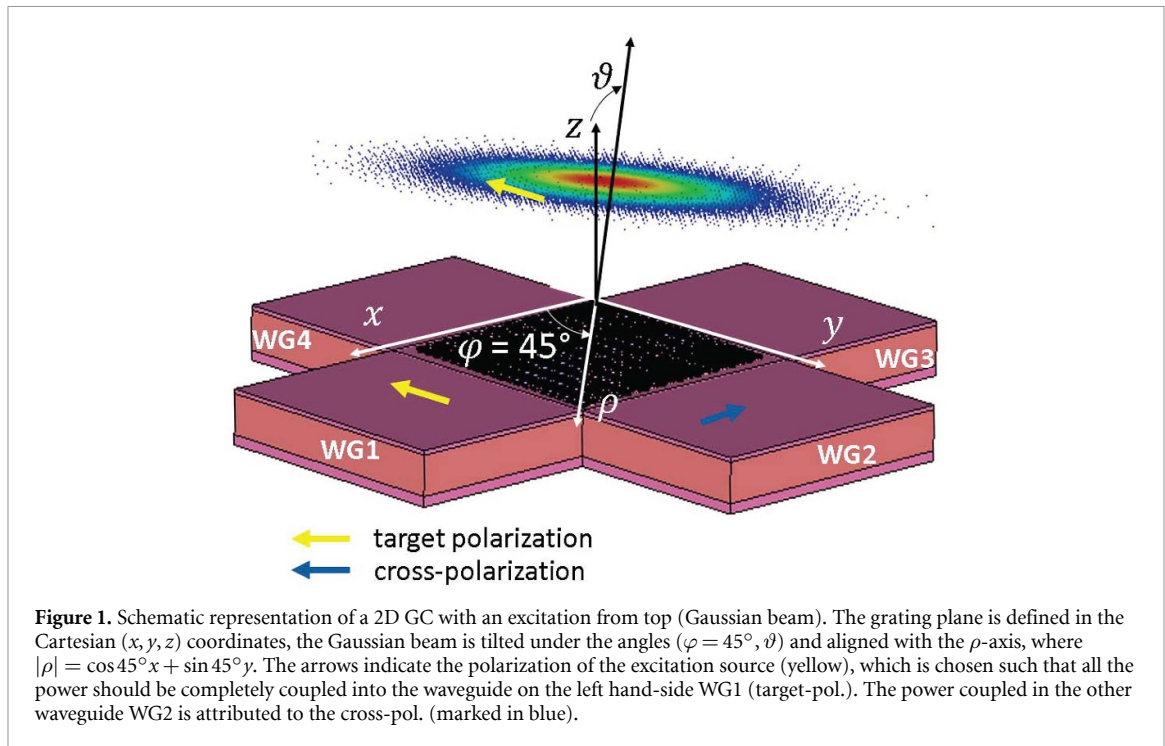
We explore scattering effects as the physical origin of cross-polarization and higher-order modes in silicon photonic 2D grating couplers (GCs). A simplified analytical model is used to illustrate that in-plane scattering always takes place, independent of grating geometry and design coupling angle. Experimental investigations show furthermore that grating design parameters are especially related to the modal composition of both the target- and the cross-polarization. Scattering effects and the associated cross-polarization and higher-order modes are indicated as the main reason for the higher 2D GC insertion loss compared to standard 1D GCs. In addition, they can be responsible for a variable 2D GC spectrum shape, bandwidth and polarization dependent loss.

1. Introduction

Silicon-based optical transmitters and receivers have been a subject of a significant research interest for many years. The main pursued objectives were cost-effectiveness and scalability, which were to be achieved by the integration of optical components on mature electronic (Bi)CMOS platforms [1, 2]. Being a popular research field over decades, silicon photonics was well-explored on component and system level with its advantages and limitations. Along with demonstrations of single devices such as coupling structures [3, 4], modulators [5, 6], multimode-interference couplers [7], 90°-hybrids [8] and photodetectors [9, 10], fully integrated transmitters [11–13] and receivers [14–18] for both direct and coherent detection have been reported. A comprehensive overview on silicon photonics for optical coherent systems going beyond communication system aspects is presented in [19].

In integrated silicon photonic devices, one of the most critical components remains the in-/out-coupling interface. In spite of the higher insertion loss, grating couplers (GCs) for nearly vertical coupling are still a popular tool, because of their simpler fabrication and coupling tolerance. However, the natural upgrade from polarization-dependent 1D GCs to polarization diversity 2D GCs is still lacking success, one of the reasons being the fact that 2D GCs are still not well-understood on a physical level. On standard 220 nm silicon-on-insulator (SOI) platforms 2D GCs show typically at least 1 dB lower coupling efficiency than standard 1D GCs (maximally −4 dB/40% vs. −3 dB/50%, see e.g. [1, 16]). Up to now, 2D GCs with around −3 dB coupling efficiency without backside mirrors could be shown on large scale only by Luxtera/STM [14], who adjusted their platform to the 2D GC requirements. Another issue is the strong polarization dependent loss (PDL), which could be solved so far without loss of efficiency only by customized scatterers' shape with a non-trivial fabrication [20, 21]. The third problem of 2D GCs occurs when they need to act as a polarization splitter and is expressed in a limited polarization split ratio between their two arms.

We devoted a previous work to the topic of the polarization split ratio limits, putting the 2D GC in the context of a receiver interface for a dual-polarization coherent transmission [22]. We showed that a 2D GC



converts a part of the power of the one basic polarization into the other orthogonal polarization. Here, we refer the properly coupled polarization as target-polarization and its converted part as cross-polarization (short: target-pol. and cross-pol.). The concept of the target- and the cross-polarizations is explained schematically in figure 1, where the field source polarization is such that all the power should be coupled in WG1 (target-pol.). The power coupled in WG2 represents the cross-pol. In [22] we showed that the cross-pol. scales with the grating perturbation strength and numerical results indicated that the cross-pol. limits not only the 2D GC splitting performance, but also its coupling efficiency.

In this letter, we investigate the in-plane scattering in 2D GCs as the physical origin of cross-polarization. As a secondary effect from scattering—higher-order mode excitation in both target- and cross-pol. results. The scattering at the grating holes is an independent process and does not have a relation to the 2D GC diffraction condition. We consider the standard case of ‘conventional’ circular holes and show experimentally that independent of grating design or coupling angle, the cross-pol. and the higher-order modes always result, even in the case of a perfectly vertical coupling. In fact, grating parameters are rather responsible for a different modal composition of the target- and cross-polarizations.

The 2D GCs considered here are designed for standard 220 nm SOI nanowire waveguides with 2 μm buried oxide thickness. For their fabrication, a standard photonic BiCMOS process is used [23, 24], which is considered for the initial 2D GC design. In spite of these specifics, our analysis on the cross-pol. and the modal composition of each polarization does not lose generality.

The paper is organized as follows. In section 2 we use a simplified analytical method to investigate mathematically the cross-pol. origins, resulting from field scattering by a dielectric cylinder, resp. by a cylinder array. In section 3 we give an overview over the experimental approach and summarize the measurement results on the presence of cross-pol. and on the excitation of higher-order modes for both target- and cross-pol. Next, we evaluate their contribution to the 2D GC insertion loss, spectrum shape, bandwidth and PDL. In the final section 4 we summarize the results and discuss possibilities to diminish or make use of the described effects.

2. Analytical methods and results

In this section, we use a simple analytical method to describe scattering by an array of dielectric cylinders and outline the limits of this approach.

GCs are typically considered as diffractive structures, for which only the diffraction condition is of interest. In 1D GCs, the grating perturbing element is defined completely along the waveguide cross-section and is continuous with respect to the wave front. Due to the weak fields at the waveguide boundaries (waveguide width typically 10 μm), diffraction is the dominant process in 1D GCs. However, in 2D GCs, the perturbing elements are discrete and have a finite dimension with respect to the waveguide and the incident

wave front. For that reason, an incident wave will not only be diffracted according to the grating diffraction condition, but also scattered in the grating plane. The scattering being initially a random process [25] can receive a more systematic nature, when the scattering elements are periodic along the propagation direction of the incident wave. This is exactly the case in 2D GCs, therefore, scattering needs to receive as much attention as diffraction. Here, we show that scattering is the effect, hiding behind cross-polarization and higher-order modes excitation, which are both not predicted by the 2D GC diffraction condition. The latter states that the polarization of a wave will be preserved and only the propagation direction will be changed according to the chosen grating period (no cross-polarization). The diffraction condition can be applied to higher-order modes, however, their refractive index is smaller and requires for the same coupling angle a significantly larger period than the 2D GCs designed for the fundamental TE₀₀ have. For that reason, higher-order modes appearing in 2D GC interfaced structures cannot result from diffraction.

Scattering of a plane wave by a dielectric or conductive cylinder has been a well-known electromagnetic problem for many years. Currently, various solutions of special cases are present in the literature. Good summaries of classical solutions were available already in the 70s [26, 27]. Simplified analyses consider the cylinder infinite in its length. In addition, the material properties include perfect metals or lossless dielectrics. In more advanced calculations, finite conductivity, dielectric losses (see e.g. [28] and the cited literature therein), anisotropy [29] or finite length [30] are taken into account. For a certain group of problems, e.g. in the optical domain, the plane wave as an incident wave is substituted by a Gaussian beam [31]. Another interesting aspect is the scattering not only by a single cylinder, but also by a periodic array [28, 31].

The grating area of a silicon photonic 2D GC combines many special conditions in its scattering nature. It consists of a dielectric cylinder array, which is periodic in two directions. The cylinders have a finite length comparable to the wavelength. The material is dielectric with a wavelength dependent refractive index. Moreover, in our case the cylinders are radially stratified, due to the BiCMOS backend of line (BEOL) filling layers. Obviously, the scattering taking place in 2D GCs is far more complex to describe than is the diffraction. A simple analytical formulation, which clearly states how the scattered field is distributed, what its propagation direction is, what polarization state(s) it has and which polarization predominates, is not available.

Here, we do not aim to derive an absolutely exact analytical description of scattering in 2D GCs, but to confirm mathematically, in a more simple configuration, that scattering is the reason for the polarization conversion in 2D GCs. We use previous analysis of the scattering properties of 2D photonic crystals [32] as a basis to illustrate that scattering always takes place in parallel to diffraction in 2D GCs. Scattering can explain the effect of what we call cross-polarization, i.e.—the partial conversion of an incident wave with a given polarization to its orthogonally polarized counterpart. The understanding of this fact is almost intuitive, since a plane wave scattered by a circular cylinder always results in a cylindrical wave. Although the cross-polarization strength depends on the scatterers' size and shape as well as on their periodicity, the occurrence of cross-polarization itself is inevitable.

For our analysis, we consider a strongly simplified case. We examine an incident plane wave instead of a Gaussian beam and let the cylinders be infinitely long. This assumption would be eligible, if a 2D GC is fully etched, the waveguide mode is very well-confined and the grating area is smaller than the waveguide width. In the following, we summarize the most important relations from [32], which are adapted to our particular problem. They represent the scattered field by a single cylinder and by a cylinder array. Since the derivations are well-explained in [32], we will omit the full details on the relations' derivation, but will outline the significant steps in the appendix.

For an incident transverse-electric (TE) wave, the magnetic field is considered parallel to the cylinder axis ($\vec{H} = H_z \vec{e}_z$) and is used for the determination of the scattered field. In general, a non-zero angle of incidence φ_i can be assumed (figure 2). The total field in the exterior is the sum of the incident and the scattered wave. Once the superposition is calculated for H_z , the electric field components result from the well-known Maxwell's equation. In figure 2 the considered cases are illustrated—figure 2(a) shows the simple case of a single cylinder, while in figure 2(b) we have the extended case of a cylinder array. In this example, the propagation direction is \vec{e}_x and the incident wave is y -polarized. We consider the refractive indices $n_{1,2}$ in the regions ① and ② and a wavelength λ . Following scattered fields result for each of the two cases:

Wave number and impedance:

$$k_1 = \frac{2\pi}{\lambda} n_1 \quad Z_1 = \sqrt{\frac{\mu_0}{\varepsilon_0 n_1^2}} \quad k_2 = \frac{2\pi}{\lambda} n_2 \quad Z_2 = \sqrt{\frac{\mu_0}{\varepsilon_0 n_2^2}}$$

$$H_z = H_0 \Psi \quad \text{TE-wave}$$

$$\Psi = \Psi^i + \Psi^s \quad i - \text{incident}, s - \text{scattered}$$

$$\Psi^i = \Phi_J^T p_0, \quad \text{with} \quad \Phi_J = [J_m(k_1 \rho) e^{jm\varphi}], \quad p_0 = [(-j)^m e^{jm\varphi_i}], \quad m = 0, \pm 1, \pm 2, \dots$$

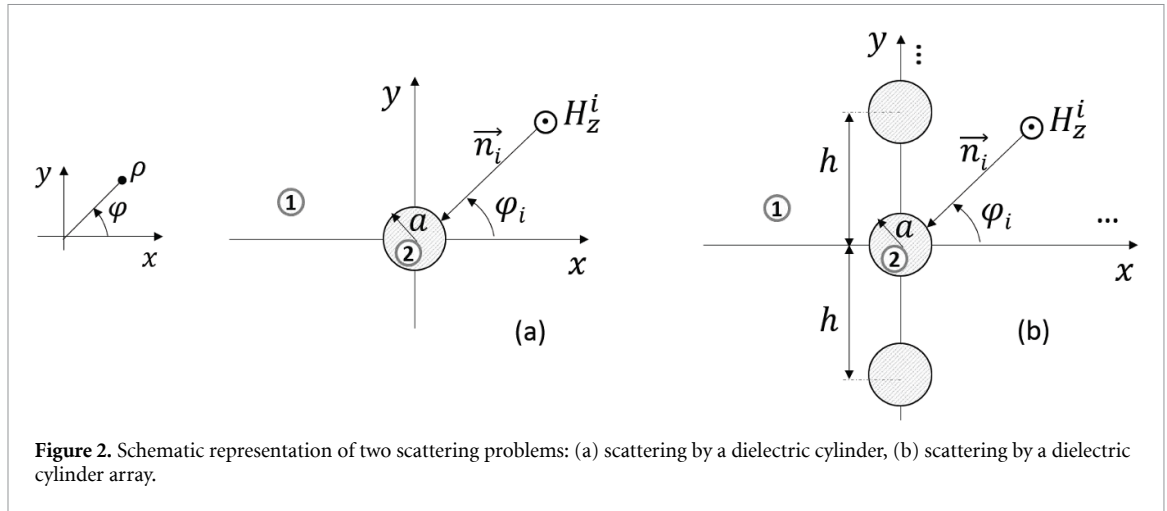


Figure 2. Schematic representation of two scattering problems: (a) scattering by a dielectric cylinder, (b) scattering by a dielectric cylinder array.

Single cylinder

$$\Psi^s = \Phi_H^T \cdot a_0^s$$

$$\Phi_H = [H_m^{(1)}(k_1 \rho) e^{jm\varphi}]$$

$$a_0^s = T p_0$$

Cylinder array

$$\Psi^s = \sum_{l=-\infty}^{\infty} e^{jk_1 \cos \varphi_i l h} \Phi_{H,l}^T a_0^s$$

$$\Phi_{H,l} = [H_m^{(1)}(k_1 \rho_l) e^{jm\varphi_l}]$$

$$\rho_l = \sqrt{x^2 + (y - lh)^2}, \quad \sin \varphi_l = \frac{y - lh}{\rho_l}$$

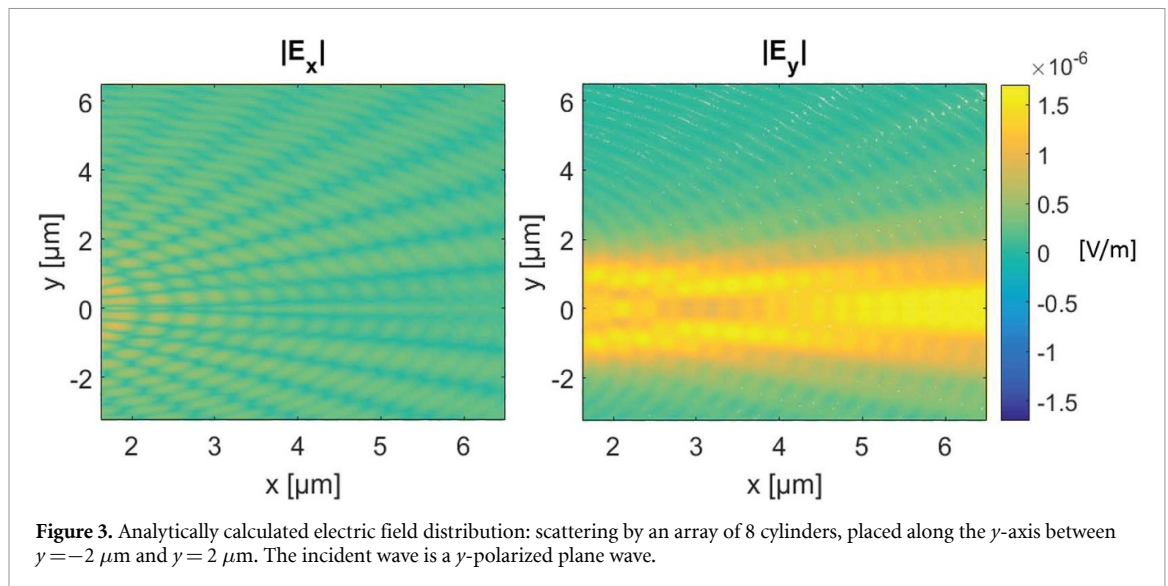
$$a_0^s = \bar{T} p_0.$$

For any of the cases, the incident wave remains the same and is only expanded in cylindrical waves, i.e. in Bessel-functions $J_m(k_1 \rho)$ with the coefficients p_0 (their sum is expressed in a vector multiplication form). The difference occurs in the scattered part: for a single cylinder, the scattered field is expressed in the sum of Hankel functions $H_m^{(1)}(k_1 \rho)$ with unknown scattering coefficients a_0^s . They can be obtained from the incident wave coefficients p_0 by using the T-matrix T [33], which results from the boundary conditions at the cylinder interface. In the periodic case, we use the Floquet-principle and superpose the contribution of each cylinder, which is the same, but spatially shifted. For the determination of the scattering coefficients, we use the aggregate T-matrix \bar{T} .

Independent of the specific case, the resulting H_z field is a cylindrical wave with both x - and y -dependence. Building the rotation of this field, we will obtain not only the initial polarization E_y , but also an E_x -polarized part, which shows clearly the origin of cross-polarization in the 2D GCs. Figure 3 shows the magnitude of the calculated E_x and E_y field components for a case, which considers the 2D GC material and geometric properties. The matrix operations are carried out in Matlab with Bessel/Hankel functions order $m = 0, \pm 1, \dots, \pm 19$. The incident plane wave has a wave front of about $5 \mu\text{m}$, the wavelength is 1550 nm . The discrete spatial locations have a resolution of 15 points per wavelength. The cylinders' material is SiO_2 , while the exterior's material is Si. The field distribution does not change significantly with the angle of incidence φ_i or with the period h . Thus, any kind of 2D GC design with cylindrical holes receives a cross-polarized field part. In this example, we choose $\varphi_i = 2^\circ$, $h = 620 \text{ nm}$ with eight periods. The cylinder radius is 220 nm . The geometric parameters are typical for previously designed 2D GCs for the C-band.

The plotted fields are scaled equally, so we can clearly see that the initial E_y -polarization predominates. The scattering at the cylinder array appears to spoil its modal purity, even if the effect is small for this short 1D array. E_x looks rather stochastically distributed without a clear propagation direction. This can be explained by the small number of scattering elements and by the missing second periodicity in propagation direction, which can enhance the E_x strength and directivity. The latter effect was observed in our previous numerical simulations reported in [22] and could not be explained by the 2D GC diffraction condition.

Discussing the limitations of the analytical model, we have to point out that the impact of the etch depth and therefore of the grating perturbation strength cannot be investigated, since we need a model considering the finite cylinder length. Due to the large index contrast in SOI, typical etch depth values for 2D GCs (e.g. 120 nm) are related to a strong perturbation strength. For that reason, the analytical solution for a completely etched array would not differ significantly from the solution for a deeply etched array. Another important point is the growing complexity, when we want to extend the model to a 2D array. In this case, the initially calculated scattered fields should be used as a new incident field on the next array. The initially weak



cross-polarized field part will be superposed constructively with the next cross-polarized field part, due to the chosen grating period. In the end, the resulting cross-pol. can become much stronger compared to a cylinder row along the y -axis (see our numerical results in [22]). The third aspect for increasing the solution accuracy is the substitution of the plane wave by a Gaussian beam. In this case, the Gaussian beam must be expanded in plane waves and the scattering problem must be solved for each partial plane wave. Obviously, the complexity of the analytical model becomes easily comparable with the one of a numerical model and loses the manageability typical for analytical representations. Nevertheless, the simplified analytical formulation is valuable as a qualitative mathematical proof of the origin of cross-polarized fields in 2D GCs.

Due to the limitations of the analytical model, we are not able to use it for the modal analysis of the target- and cross-pol. A numerical approach would require a 2D GC excitation from top, which results in a very large model. Aside from computational time and memory requirements, we are also limited in the number of wavelength points, which can be stored during the calculation. In addition, all results depend on the position of the excitation source, which requires multiple sweeps. For these reasons, we have chosen an experimental approach for the higher-order modes investigation, which will be explained in the next section.

3. Experimental methods and results

In our experiment, we investigate the excitation of the TE_{00} and the higher TE_{10} mode in three different 2D GC designs, considering both the target- and the cross-pol.

The first aspect of our analysis is the coupling position dependence of the extinction ratio (ER) between the target-pol. TE_{00} and the remaining polarizations/modes. The reason for this analysis is the fact that in integrated devices the exact fiber alignment at the symmetry plane of a 2D GC is difficult and thus the coupling to the two GC arms may look differently. In particular, higher-order TE_{10} mode coupling may be a problem, since in single-mode waveguides the TE_{10} mode will simply result in excess loss. We consider target- and cross-pol. TE_{10} as well as cross-pol. TE_{00} as a consequence of scattering. The target-pol. TE_{00} results from diffraction. If the central wavelength of TE_{10} is in the vicinity of the target TE_{00} central wavelength and we have an imbalance of TE_{10} in the 2D GC arms, we will observe PDL. If TE_{10} is centered at a shifted wavelength, the signals' spectral shape and bandwidth will be influenced. So, signals in the two 2D GC arms may have different 1 or 3 dB bandwidths. At last, the coupling position dependence of the cross-pol. TE_{00} can give us insight in the split ratio (i.e. the ratio between the fundamental target- and cross-pols) variation, which is relevant for 2D GCs used in coherent transceivers.

The second aspect is the impact of wafer variations on the TE_{00} and TE_{10} modes of the target- and cross-pol, which is relevant for the repeatability of the device behavior. For our statistics, we consider nine arbitrarily chosen chips on the wafer and compare the three considered 2D GC designs.

3.1. Experimental approach and setup

3.1.1. Test structures

All test structures are fabricated in a photonic BiCMOS [23, 24] short flow, in which the BEOL was not completely processed. This is eligible for the current investigation, since the BEOL has no impact on the mode excitation by the 2D GCs and its omission reduces significantly the fabrication time. The minimum

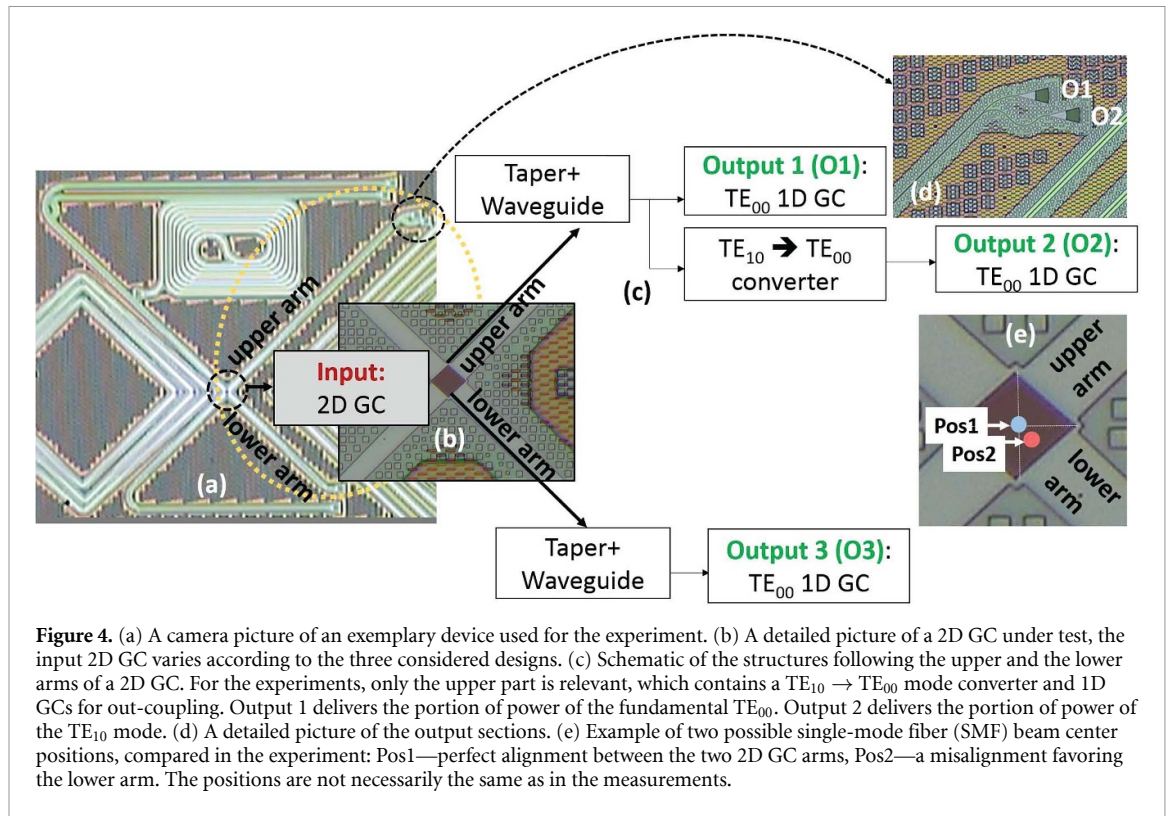


Figure 4. (a) A camera picture of an exemplary device used for the experiment. (b) A detailed picture of a 2D GC under test, the input 2D GC varies according to the three considered designs. (c) Schematic of the structures following the upper and the lower arms of a 2D GC. For the experiments, only the upper part is relevant, which contains a TE₁₀ → TE₀₀ mode converter and 1D GCs for out-coupling. Output 1 delivers the portion of power of the fundamental TE₀₀. Output 2 delivers the portion of power of the TE₁₀ mode. (d) A detailed picture of the output sections. (e) Example of two possible single-mode fiber (SMF) beam center positions, compared in the experiment: Pos1—perfect alignment between the two 2D GC arms, Pos2—a misalignment favoring the lower arm. The positions are not necessarily the same as in the measurements.

Table 1. 2D GC designs used for the investigation of the target- and cross-pol. modal composition.

Abbr.	Coupling angle	Shear angle	Grating period (nm)	Holes diameter (nm)	Etch depth (nm)
M1	0°	0°	585	360	120
M3	8°	2°, Type I	622	440	120
M4	8°	2°, Type II	622	440	120

feature size is defined by the 248 nm deep UV lithography we used. Figure 4(a) shows an exemplary device picture taken with a microscope camera, the relevant device parts are indicated by the dashed ellipse in yellow. Figure 4(b) shows a more detailed picture of a 2D GC under test. Figure 4(c) illustrates schematically the structures in the upper and the lower arms of the 2D GC. Only the upper arm is relevant for the experiments. There, we apply after down-tapering a TE₁₀ → TE₀₀ mode converter, which can extract a TE₁₀ mode propagating in the waveguide towards Output 1 (O1) and convert it to the fundamental TE₀₀ propagating into the waveguide towards Output 2 (O2). Therefore, for the polarization in question, O1 gives us information about the power coupled into the fundamental mode TE₀₀, while O2 shows the share of TE₁₀. At each output, identical focusing 1D GCs are used (period 610 nm, duty cycle 0.52, etch depth 70 nm, design coupling angle 8°). Figure 4(d) shows a detailed camera picture of the output sections.

Three different 2D GC designs are compared during the measurements. The first one is intended for a zero angle of incidence ϑ (see figure 1) and has no waveguide-to-grating shear angle. The other two are designed for a 8° coupling angle ϑ and differ by the realization of their waveguide-to-grating shear angle. A sheared 2D GC of Type I has orthogonal waveguides and rhombus-shaped grating area. A sheared 2D GC of Type II has angled waveguides and square shaped grating area. The geometrical details are summarized in table 1 listed with their abbreviations that will be used to refer to the structures.

The TE₁₀ → TE₀₀ mode converter consists of multiple adiabatic taper sections, which are designed as in Ref [34]. The conversion efficiency of TE₁₀ to TE₀₀ (O2) is better than 98.6% (−0.06 dB) for the whole C-band. The portion of TE₁₀ power further propagating towards O1 is less than 1‰ (−30 dB). The fundamental TE₀₀ arrives at O1 with an efficiency better than 99.6% (−0.02 dB) and less than 4.5‰ (−23.5 dB) can couple down and propagate towards O2.

3.1.2. Experimental setup and approach

We perform manual wafer measurements. Our setup consists of a tunable laser source Agilent 81940A, followed by a manual polarization controller. Standard single-mode fibers (SMFs) are used for the in- and out-coupling. The measured signal is detected by a power meter Agilent 81634B.

We observed a strong dependence of the mode power magnitude, depending on the coupling position. This is well explainable, since it is difficult to place the SMF exactly at the 2D GC symmetry plane between its two arms. For that reason, we show here measurements comparing two different coupling positions. The first one (Pos1) is for optimal coupling in the O1 arm, which gives us an idea of the maximal possible higher-order mode coupling. Another position (Pos2), which is less optimal for the O1 arm shows possible deviations caused by the coupling misalignment. The vertical distance is in both cases the same. Figure 4(e) shows an example of two possible positions of the SMF fiber beam center: Pos1 (exactly between the two 2D GC arms) and Pos2 (favoring the lower arm). The positions drawn are only an example and are not necessarily the same as in the measurement. For the optimal position, the measurement steps are as follows:

- Position and polarization at the 2D GC adjusted for a maximal out-coupling at O1:
 - measure the signal at O1, corresponding to TE_{00} for the target-polarization,
 - measure the signal at O2, corresponding to TE_{10} for the target-polarization.
- Position kept constant and polarization at the 2D GC adjusted for a minimal out-coupling at O1:
 - measure the signal at O1, corresponding to TE_{00} for the cross-polarization,
 - measure the signal at O2, corresponding to TE_{10} for the cross-polarization.

For the measurement at a non-optimal position, the alignment at the 2D GC plane is such that the out-coupling efficiency at O1 is reduced between 2 and 3 dB. With this position, the steps given above are repeated. For each structure, we compare the ER between the target-pol. TE_{00} and the remaining polarizations/modes at the two positions and look whether it remains constant. For the ER estimation, we consider two wavelengths—the maximum transmission wavelength of the target-pol. TE_{00} or the maximum transmission wavelength of the other polarization/mode.

In a second measurement, we adjust the position for a maximal out-coupling at O1 and perform statistical measurements on nine chips on the wafer, by only changing the polarization, according to the steps given above (maximal or minimal transmission at O1). The mean ER of the target-pol. TE_{00} vs. the remaining polarizations/modes at the mean central wavelength of the target-pol. TE_{00} gives us insight in the insertion loss variations due to higher-order modes and cross-pol. The mean ER calculated at the central wavelengths of the other polarizations/modes shows the 2D GC spectrum shape and bandwidth variation due to fabrication deviations. This information is used to compare M1, M3 and M4. For the statistical measurements, we intentionally choose a larger coupling distance, in order to exclude the distance variation as a factor and to move easily from one chip to another on the wafer. The insertion loss (in- and out-coupling) is between 4 and 5 dB higher than for the case of an optimal coupling height.

3.2. Experimental results and discussion

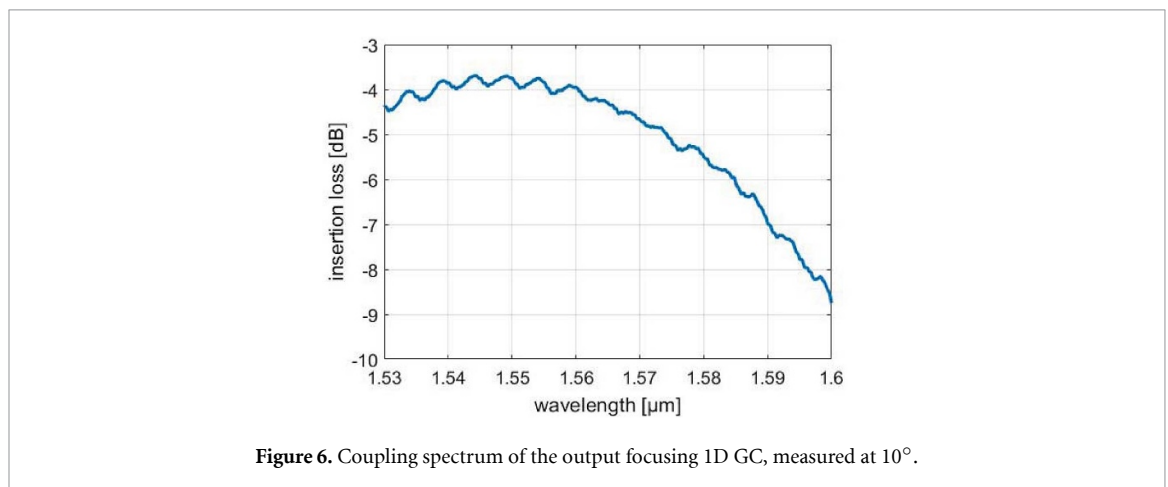
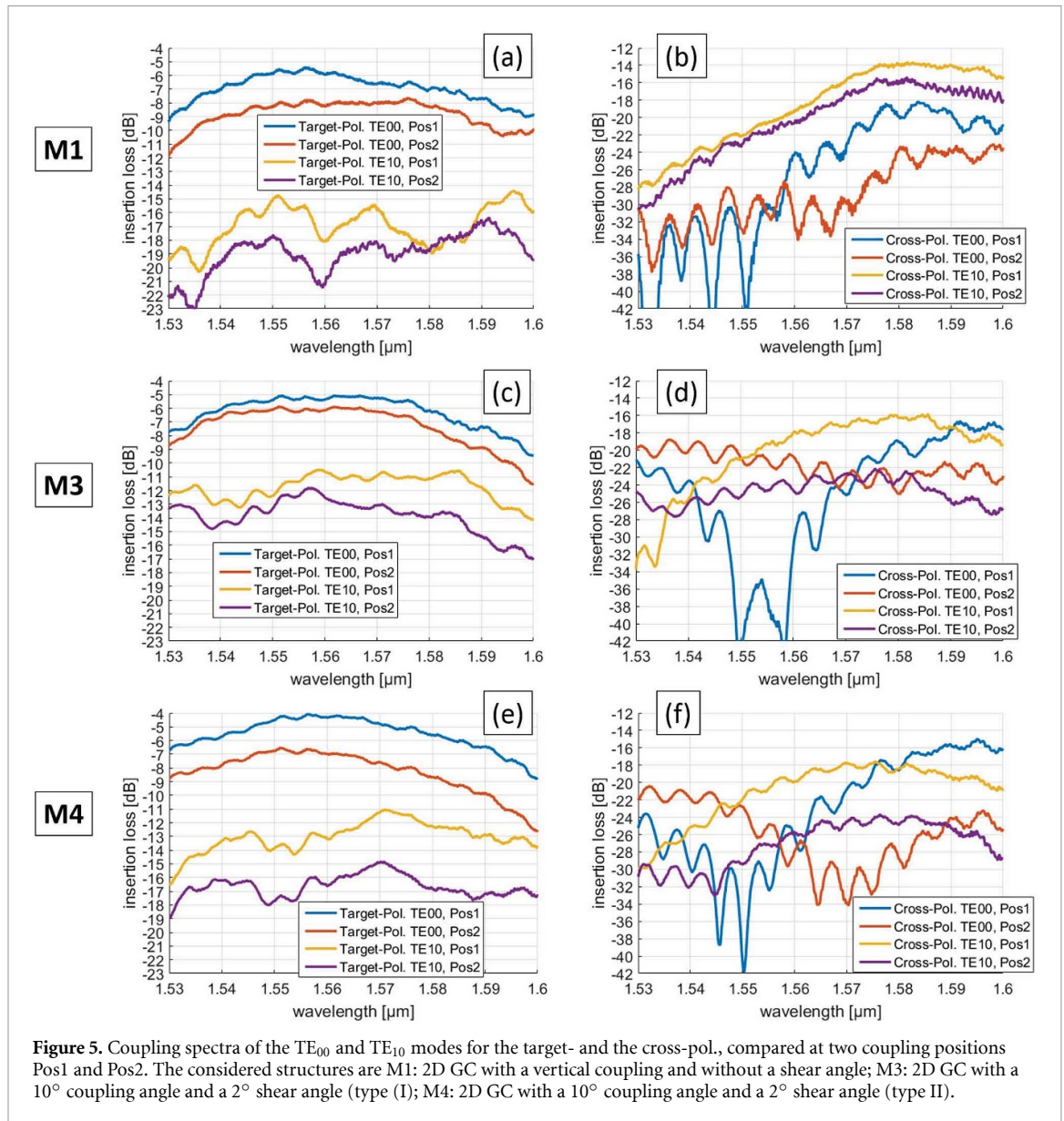
First experimental results indicated a refractive index deviation from the design value. For that reason, the 1D GCs, as well as the 2D GCs M3 and M4 showed a coupling angle of 10° (instead of 8°). The coupling angle of M1 was 0° .

3.2.1. Investigation of the coupling position

Figures 5(a)–(f) shows the coupling spectra of the TE_{00} and TE_{10} modes for the target- and the cross-pol., compared at the two positions Pos1 and Pos2. The positions Pos1 and Pos2 for the three different structures M1, M3, M4 are not comparable with each other. The figures on the left column refer to the target-pol., while the cross-pol. is displayed on the right column. From top to bottom, the structures' sequence is M1, M3 and M4. The insertion loss is determined by subtracting the input power of around 6 dBm as well as the insertion loss of the 1D GC. The 1D GC coupling spectrum is shown in figure 6.

In all subfigures in figure 5 it is evident that cross-pol. with its shares of TE_{00} and TE_{10} , as well as target-pol. TE_{10} are present in every considered structure, reaching levels of more than -20 dB. While the target-pol. TE_{10} has a wavier and rather flat spectrum, the cross-pol. mode components have mostly a well pronounced maximum. Looking at the first structure M1 with a vertical coupling, we see that the cross-pol. TE_{00} and TE_{10} are centered at nearly the same wavelength. All polarizations and modes improve their coupling efficiency with the optimal position Pos1, meaning that it is rather difficult to find a position, where the target-pol. TE_{00} is well coupled and the other polarizations/modes not. Looking at the structures M3 and M4, we see that the coupling efficiency scaling with the position optimization is still present, except for the case cross-pol. TE_{00} . The latter shows strongly varying minimums and maximums, but for the optimal case, the minimum is well below the maximum of the target-pol. TE_{00} . The coupling maximums of the cross-pol. TE_{00} and TE_{10} are this time about 20–30 nm wavelength shifted from each other.

Tables 2, 3 and 4 show the ER of the target-pol. TE_{00} vs. target-pol. TE_{10} , cross-pol. TE_{00} and cross-pol. TE_{10} for M1, M3 and M4 respectively. Comparing results at different positions, we see that at a fixed



wavelength, the target-pol. TE₁₀ changes by no more than 2 dB for M1 and by no more than 1 dB for M3 and M4. On the other hand, the cross-pol. TE₀₀ varies stronger with the position. An optimized position reduces the cross-pol. TE₀₀ at the maximum of the target-pol. TE₀₀. In the same time, the cross-pol. TE₀₀ strength increases at its maximum transmission wavelength. In structures M3 and M4, the cross-pol. TE₁₀ shows the

Table 2. Extinction ratios between the target-pol. TE₀₀ and the other considered polarizations/modes for the structure M1. The first evaluation wavelength in the rows 1–3 is the maximum transmission wavelength of the target TE₀₀. The next wavelengths are the corresponding maximum transmission wavelengths of target-pol. TE₁₀, cross-pol. TE₀₀ and cross-pol. TE₁₀.

ER (dB) Target-pol. TE ₀₀ vs.	Pos2	Pos1	1. Wavelength (μm)
Target-pol. TE ₁₀	12.6	10.6	1.5558
Cross-pol. TE ₀₀	23.2	27.3	1.5558
Cross-pol. TE ₁₀	13.4	15	1.5558
2. Wavelength (μm)			
Target-pol. TE ₁₀	11	10.2	1.5700
Cross-pol. TE ₀₀	15	9	1.6026
Cross-pol. TE ₁₀	6.7	6	1.5785

Table 3. Extinction ratios between the target-pol. TE₀₀ and the other considered polarizations/modes for the structure M3. The first evaluation wavelength in the rows 1–3 is the maximum transmission wavelength of the target TE₀₀. The next wavelengths are the corresponding maximum transmission wavelengths of target-pol. TE₁₀, cross-pol. TE₀₀ and cross-pol. TE₁₀.

ER (dB) Target-pol. TE ₀₀ vs.	Pos2	Pos1	1. Wavelength (μm)
Target-pol. TE ₁₀	7.2	6.1	1.5670
Cross-pol. TE ₀₀	16.5	19.4	1.5670
Cross-pol. TE ₁₀	17.6	11.8	1.5670
2. Wavelength (μm)			
Target-pol. TE ₁₀	6.5	5.2	1.5710
Cross-pol. TE ₀₀	13.9	9.5	1.5910
Cross-pol. TE ₁₀	16	9	1.5856

Table 4. Extinction ratios between the target-pol. TE₀₀ and the other considered polarizations/modes for the structure M4. The first evaluation wavelength in the rows 1–3 is the maximum transmission wavelength of the target TE₀₀. The next wavelengths are the corresponding maximum transmission wavelengths of target-pol. TE₁₀, cross-pol. TE₀₀ and cross-pol. TE₁₀.

ER (dB) target-pol. TE ₀₀ vs.	Pos2	Pos1	1. Wavelength (μm)
Target-pol. TE ₁₀	9.8	9.2	1.5564
Cross-pol. TE ₀₀	19.1	24.7	1.5564
Cross-pol. TE ₁₀	21.2	15.8	1.5564
2. Wavelength (μm)			
Target-pol. TE ₁₀	6.8	6	1.5713
Cross-pol. TE ₀₀	12.2	7.5	1.5942
Cross-pol. TE ₁₀	15.5	12.4	1.5757

opposite behavior at the considered wavelengths. For M1, the cross-pol. TE₁₀ position dependence is small. The optimal position for a non-zero angle coupling is required for a good split ratio at the target-pol. central wavelength (cross-pol. TE₀₀ low), but the loss contribution of the target- and cross-pol. TE₁₀ increases in the same time. The good split ratio is achievable at the cost of more loss, caused by higher-order modes.

The cross-pol. TE₁₀ has a shifted central wavelength and its coupling strength variation with the position can cause a variable bandwidth of the signals in the 2D GC arms. On the other hand, the target-pol. TE₁₀ reaches a high coupling efficiency near the maximum transmission wavelength of the target-pol. TE₀₀. Its imbalanced position will cause PDL, because the coupled power of TE₁₀ in the two 2D GC arms will be different. In the case of a low misalignment, the target-pol. TE₁₀ will simply contribute to the insertion loss in both 2D GC waveguides.

3.2.2. Investigation of wafer variations

The wafer-level behavior of the structures M1, M3 and M4 are summarized in tables 5, 6 and 7. Similarly, we calculated the mean ER of the target-pol. TE₀₀ against target-pol. TE₁₀, cross-pol. TE₀₀ and cross-pol. TE₁₀. The evaluation wavelengths are the mean maximum transmission wavelength of target-pol. TE₀₀ (the first three rows), followed by the mean maximum transmission wavelength of target-pol. TE₁₀, cross-pol. TE₀₀ and cross-pol. TE₁₀. The given ERs are averaged over nine chips and the standard deviation σ is given as well.

Table 5. Mean extinction ratios $\pm\sigma$ between the target-pol. TE₀₀ and the other considered polarizations/modes for the structure M1, averaged over nine chips. The first evaluation wavelength in the rows 1–3 is the mean maximum transmission wavelength of the target TE₀₀. The next wavelengths are the corresponding mean maximum transmission wavelengths of target-pol. TE₁₀, cross-pol. TE₀₀ and cross-pol. TE₁₀.

Target-pol. TE ₀₀ vs.	Mean ER $\pm\sigma$ (dB)	1. Wavelength (μm)
Target-pol. TE ₁₀	10.5 \pm 1.9	1.5519
Cross-pol. TE ₀₀	29.6 \pm 2.0	1.5519
Cross-pol. TE ₁₀	17.3 \pm 0.9	1.5519
2. Wavelength (μm)		
Target-pol. TE ₁₀	10.6 \pm 1.9	1.5525
Cross-pol. TE ₀₀	13.3 \pm 2.3	1.5755
Cross-pol. TE ₁₀	5.3 \pm 1.3	1.5785

Table 6. Mean extinction ratios $\pm\sigma$ between the target-pol. TE₀₀ and the other considered polarizations/modes for the structure M3, averaged over nine chips. The first evaluation wavelength in the rows 1–3 is the mean maximum transmission wavelength of the target TE₀₀. The next wavelengths are the corresponding mean maximum transmissions wavelength of target-pol. TE₁₀, cross-pol. TE₀₀ and cross-pol. TE₁₀.

Target-pol. TE ₀₀ vs.	Mean ER $\pm\sigma$ (dB)	1. Wavelength (μm)
Target-pol. TE ₁₀	12.7 \pm 2.6	1.5586
Cross-pol. TE ₀₀	24.9 \pm 3.7	1.5586
Cross-pol. TE ₁₀	17 \pm 3.1	1.5586
2. Wavelength (μm)		
Target-pol. TE ₁₀	12.7 \pm 2.6	1.5583
Cross-pol. TE ₀₀	4.6 \pm 1.7	1.5919
Cross-pol. TE ₁₀	12 \pm 0.6	1.5767

Table 7. Mean extinction ratios $\pm\sigma$ between the target-pol. TE₀₀ and the other considered polarizations/modes for the structure M4, averaged over nine chips. The first evaluation wavelength in the rows 1–3 is the mean maximum transmission wavelength of the target TE₀₀. The next wavelengths are the corresponding mean maximum transmission wavelengths of target-pol. TE₁₀, cross-pol. TE₀₀ and cross-pol. TE₁₀.

Target-pol. TE ₀₀ vs.	Mean ER $\pm\sigma$ (dB)	1. Wavelength (μm)
Target-pol. TE ₁₀	11.6 \pm 2.2	1.5587
Cross-pol. TE ₀₀	27.5 \pm 7.5	1.5587
Cross-pol. TE ₁₀	17.3 \pm 1.5	1.5587
2. Wavelength (μm)		
Target-pol. TE ₁₀	11.5 \pm 2.4	1.5594
Cross-pol. TE ₀₀	4.7 \pm 1.2	1.5915
Cross-pol. TE ₁₀	11.9 \pm 1.1	1.5763

The target-pol. TE₁₀ is for both considered wavelengths of similar level for all structures with a maximal ER difference of 2 dB between M1 and M3. The target-pol. modal composition has therefore smaller dependence on the 2D GC design parameters. The cross-pol. TE₀₀ and TE₁₀ at the central wavelength of the target-pol. TE₀₀ are also of similar order. However, when we look at their maximum transmission wavelengths, we see that in M1, the cross-pol. TE₁₀ predominates and the mean ER is around 7 dB smaller than those of M3 and M4. On contrary, for M3 and M4 the cross-pol. TE₀₀ predominates with about 8 dB smaller ER than for M1. This observation shows that the 2D GC design parameters are responsible for the cross-pol. modal composition.

Finally, we can estimate the mean loss contribution of the higher-order TE₁₀ of the target- and cross-pol., evaluated from the ERs at the central wavelength of the target-pol. TE₀₀. For that purpose, we calculate the higher-order modes overall percentage of the normalized in-coupled power. For M1, we obtain about 10%, for M3 7% and for M4 8%. Since this power percentage will be lost due to the single-mode waveguides, it can explain to some extent the overall lower coupling efficiency of the 2D GCs on standard SOI compared to their 1D counterparts. Their difference is roughly in the range 40% vs. 50%.

4. Summary and conclusions

In this work, we performed analysis on fundamental physical effects in 2D GCs on two levels. First, we used an analytical method to show that in any kind of 2D GC, scattering at the cylindrical grating holes takes place in parallel with diffraction. Scattering is a natural explanation for the polarization conversion of a given target polarization and the occurrence of cross-polarization. In addition, scattering can be responsible for a modal impurity of both polarizations. Since the analytical method is very limited, we continued in the next step with experimental investigations on the modal composition of the target- and cross-polarization. The higher-order mode TE_{10} was considered as a source of additional loss, due to the single-mode waveguides used.

In a first measurement we could confirm that along with the target-polarized TE_{00} a higher-order target-polarized TE_{10} as well as cross-polarized TE_{00} and TE_{10} modes are excited by the three considered 2D GC designs. Next, we evaluated different coupling positions to find out, whether the ratio between the target-polarized TE_{00} and the target-polarized TE_{10} , cross-polarized TE_{00} and cross-polarized TE_{10} remains constant. The different positions account for the case of imbalance between the 2D GC arms, when the coupling position is not perfectly aligned at the 2D GC symmetry plane. We found out, that the target-polarized TE_{10} occurs near the central wavelength of the target-polarized TE_{00} . For that reason, its coupling position dependence can lead to an increased PDL between two imbalanced signals in the 2D GC arms. The cross-polarized TE_{10} is shifted to larger wavelengths and its position dependence can lead to different bandwidths of two imbalanced 2D GC signals. The cross-polarized TE_{00} maximum is shifted to larger wavelengths as well, making the 2D GC polarization crosstalk less vulnerable against position variations.

Next, we compared statistically the three 2D GC designs, by performing wafer-scale measurements. While the target-polarized TE_{10} has for all structures a similar level and variation range, the cross-polarized modal compositions have a stronger design dependence. A zero in-coupling angle leads to a stronger cross-polarization TE_{10} coupling, while structures with a non-zero in-coupling angle show more fundamental cross-polarization TE_{00} . The 2D GC design is responsible for the modal composition of the cross-polarization. At last, we estimated the mean loss contribution of the higher-order modes of both polarizations at the central transmission wavelength of the target TE_{00} . We found between 7% and 10% additional loss for the three designs, which can explain the overall higher insertion loss of 2D GCs compared to 1D GCs.

Most effects described above are highly undesirable. For certain applications like inter-modal four-wave mixing the polarization and mode diversity may be of interest. However, in telecommunications, the 2D GCs can find realization only if they become more competitive. Recognizing their fundamental limitations is the first optimization step. Obviously, scattering in 2D GCs is a crucial problem. Scattering needs to be kept as low as possible. However, this is not a trivial task. The special scatterers' shape proposed by Luxtera is not a solution for every lithographic technique. A possibility for reducing the scattering could be to go for apodized gratings. In this case, each hole has a different size and the spacing between the holes varies in order to keep the effective refractive index constant. This could reduce the constructive superposition of the scattered fields by each single hole. Future work will focus on the investigation of this possible solution and will investigate whether this can be repeatably realized on larger-scale.

Data availability statement

The data that support the findings of this study are available upon reasonable request from the authors.

Acknowledgement

The authors acknowledge partial support from the Federal Ministry of Education and Research, Project No. BMBF 13N14936 (PEARLS) and the German Research Foundation, Project Nos. DFG ZI 1283-5-1 (ULTRA) and DFG ZI 1283-6-1-(EPIC-Sense).

Appendix A.

For our calculations, we start with a single cylinder (figure 2(a)), which will be later extended to a cylinder array (figure 2(b)). In the first half-space, the incident wave and later the scattered wave have a wave number k_1 and the wave impedance Z_1 , depending on the material refractive index n_1 . In our case, n_1 is the Si waveguide effective refractive index. In the cylinder with a radius a , we have the refractive index n_2 , for which

we assume SiO₂, with the corresponding wave number k_2 and wave impedance Z_2 :

$$k_1 = \frac{2\pi}{\lambda} n_1 \quad Z_1 = \sqrt{\frac{\mu_0}{\varepsilon_0 n_1^2}} \quad k_2 = \frac{2\pi}{\lambda} n_2 \quad Z_2 = \sqrt{\frac{\mu_0}{\varepsilon_0 n_2^2}},$$

with λ the free space wavelength.

The incident plane wave is considered to be TE, with the only magnetic field component H_z parallel to the cylinder axis, which is used for all following calculations. In general, the wave has a nonzero angle of incidence φ_i , which can be related to a waveguide-grating shear angle. The first step is to expand the incident plane wave in a sum of cylindrical waves (Jacobi–Anger identity), which can be written in matrix form. Here, $[\cdot]$ represents a column vector with m -elements.

$$H_z = H_0 e^{-jk_1(\cos \varphi_i x + \sin \varphi_i y)} = H_0 e^{-jk_1 \rho \cos(\varphi - \varphi_i)} = H_0 \Psi^i(\rho, \varphi),$$

$$\Psi^i(\rho, \varphi) = \Phi_J^T \cdot p_0 \quad \text{with} \quad \Phi_J = [J_m(k_1 \rho) e^{jm\varphi}], \quad p_0 = [(-j)^m e^{jm\varphi_i}], \quad m = 0, \pm 1, \pm 2, \dots,$$

The scattered field can be expressed as a sum of Hankel functions of first kind, weighted by unknown scattering coefficients a_0^s :

$$\Psi^s = \Phi_H^T \cdot a_0^s \quad \text{with} \quad \Phi_H = [H_m^{(1)}(k_1 \rho) e^{jm\varphi}].$$

The scattering coefficients are related to the incident wave coefficients by the T-Matrix T [33], which results from the continuity condition at the cylinder surface. For a TE-wave the T-Matrix is given as:

$$T = [\tau_m \delta_{mn}], \quad \text{with} \quad \tau_m = -\frac{Z_2 J_m(k_1 a) J_m'(k_2 a) - Z_1 J_m(k_2 a) J_m'(k_1 a)}{Z_2 J_m'(k_2 a) H_m^{(1)}(k_1 a) - Z_1 J_m(k_2 a) H_m^{(1)'}(k_1 a)},$$

$$a_0^s = T p_0,$$

with δ_{mn} the Kronecker's delta. Now, we extend the solution for a single cylinder to a h -periodic cylinder array along the y -axis (figure 2(b)), using the Floquet principle. The scattered field is now modified as:

$$\Psi^s(x, y) = \sum_{l=-\infty}^{\infty} e^{jk_1 \cos \varphi_i l h} \Phi_{H,l}^T a_0^s \quad \text{with}$$

$$\Phi_{H,l} = [H_m^{(1)}(k_1 \rho_l) e^{jm\varphi_l}], \quad \rho_l = \sqrt{x^2 + (y - lh)^2}, \quad \sin \varphi_l = \frac{y - lh}{\rho_l}.$$

The T-Matrix T will be substituted by the aggregate T-matrix \bar{T} with the following steps:

$$L = [L_{mn}], \quad L_{mn} = \sum_{l=1}^{\infty} H_{n-m}^{(1)}(k_1 l h) \left[e^{-jk_1 \cos \varphi_i l h} + (-1)^{n-m} e^{jk_1 \cos \varphi_i l h} \right]$$

$$\bar{T} = (I - TL)^{-1} T$$

$$a_0^s = \bar{T} p_0.$$

The final field outside the cylinder is a superposition of the incident and scattered waves. The corresponding electric field can be obtained by the well-known Maxwell's equation:

$$\Psi(x, y) = \Phi_J^T p_0 + \sum_{l=-\infty}^{\infty} e^{jk_1 \cos \varphi_i l h} \Phi_{H,l}^T a_0^s$$

$$\vec{H} = H_0 \Psi(x, y) \vec{e}_z$$

$$\vec{E} = \frac{1}{j\omega \varepsilon_0 n_1^2} \text{rot } \vec{H}.$$

ORCID iD

Galina Georgieva  <https://orcid.org/0000-0003-2693-8147>

References

- [1] Zimmermann L *et al* 2015 BiCMOS silicon photonics platform *Optical Fiber Conf.* OSA Technical Digest (online) (Optical Society of America) paper Th4E.5
- [2] Mekis A *et al* 2012 A CMOS photonics platform for high-speed optical interconnects *IEEE Photonics Conf., 2012 (Burlingame, CA)* pp 356–7
- [3] Taillaert D *et al* 2006 Grating couplers for coupling between optical fibers and nanophotonic waveguides *Japan. Appl. Phys.* **45** 6071
- [4] Tsuchizawa T *et al* 2005 Microphotonics devices based on silicon microfabrication technology *IEEE J. Sel. Top. Quantum Electron.* **11** 232–40
- [5] Thomson D J *et al* 2012 50-Gb/s silicon optical modulator *IEEE Photonics Technol. Lett.* **24** 234–6
- [6] Rito P *et al* 2016 A monolithically integrated segmented linear driver and modulator in EPIC 0.25- μ m SiGe:C BiCMOS platform *IEEE Trans. Microw. Theory Tech.* **64** 4561–72
- [7] Sheng Z *et al* 2012 A compact and low-loss MMI coupler fabricated with CMOS technology *IEEE Photon. J.* **4** 2272–7
- [8] Voigt K, Zimmermann L, Winzer G, Tian H, Tillack B and Petermann K 2011 C-band optical 90° hybrids in silicon nanowaveguide technology *IEEE Photonics Technol. Lett.* **23** 1769–71
- [9] DeRose C T *et al* 2011 Ultra compact 45 GHz CMOS compatible Germanium waveguide photodiode with low dark current *Opt. Express* **19** 24897–904
- [10] Lischke S *et al* 2014 High-speed, waveguide Ge PIN photodiodes for a photonic BiCMOS process 2014 *IEEE Bipolar/BiCMOS Circuits and Technology Meeting (BCTM)* (Coronado, CA) pp 29–32
- [11] Xiong C, Gill D, Proesel J, Orcutt J, Haensch W and Green W M J 2015 A monolithic 56 Gb/s CMOS integrated nanophotonic PAM-4 transmitter 2015 *IEEE Optical Conf. (OI)* (San Diego, CA) pp 16–7
- [12] Petousi D *et al* 2016 High-speed monolithically integrated silicon photonic transmitters in 0.25 μ m BiCMOS platform *ECOC 2016 (Dusseldorf, Germany)* pp 604–6
- [13] Shastri A *et al* 2014 Experimental demonstration of ultra-low-power single polarization 56 Gb/s QAM-16 generation without DAC using CMOS photonics 2014 *Conf. Optical Communication (ECOC)* (Cannes) pp 1–3
- [14] Boeuf F *et al* 2013 A multi-wavelength 3D-compatible silicon photonics platform on 300mm SOI wafers for 25 Gb/s applications 2013 *IEEE Int. Electron Devices Meeting (Washington, DC)* p 13.3.1–4
- [15] Gudyriev S *et al* 2016 Low-power, ultra-compact, fully-differential 40 Gbps direct detection receiver in 0.25 μ m photonic BiCMOS SiGe technology 2016 *IEEE 13th Int. Conf. Group IV Photonics (GFP)* (Shanghai) pp 178–9
- [16] Doerr C R *et al* 2010 Monolithic polarization and phase diversity coherent receiver in silicon *J. Lightwave Technol.* **28** 520–5
- [17] Painchaud Y *et al* 2013 Ultra-compact coherent receiver based on hybrid integration on silicon 2013 *Optical Fiber Conf. and Exposition and the National Fiber Optic Conf. (OFC/NFOEC)* (Anaheim, CA) pp 1–3
- [18] Winzer G *et al* 2015 Monolithic photonic-electronic QPSK receiver for 28Gbaud 2015 *Optical Fiber Conf. and Exhibition (OFC)* (Los Angeles, CA) pp 1–3
- [19] Doerr C and Chen L 2018 Silicon photonics in optical coherent systems *Proc. IEEE* **106** 2291–301
- [20] Mekis A *et al* 2011 A grating-coupler-enabled CMOS photonics platform *IEEE J. Sel. Top. Quantum Electron.* **17** 597–608
- [21] Plantier S, Fowler D, Hassan K, Lemonnier O and Orobitchouk R 2016 Impact of scattering element shape on polarisation dependent loss in two dimensional grating couplers 2016 *IEEE 13th Int. Conf. Group IV Photonics (GFP)* (Shanghai) pp 76–7
- [22] Georgieva G *et al* 2020 Cross-polarization effects in sheared 2D grating couplers in a photonic BiCMOS technology *Japan. J. Appl. Phys.* **59** SOOB03
- [23] Knoll D *et al* 2015 High-performance photonic BiCMOS process for the fabrication of high-bandwidth electronic-photonic integrated circuits 2015 *IEEE Int. Electron Devices Meeting (IEDM)* (Washington, DC) pp 15.6.1–4
- [24] Knoll D *et al* 2016 BiCMOS silicon photonics platform for fabrication of high-bandwidth electronic-photonic integrated circuits 2016 *IEEE 16th Topical Meeting on Silicon Monolithic Integrated Circuits in RF Systems (SiRF)* (Austin, TX) pp 46–9
- [25] Gouesbet G and Grehan G 2011 *Generalized Lorenz-Mie Theories* (Berlin: Springer)
- [26] Kerker M 1969 *The Scattering of Light* (New York: Academic)
- [27] Bowman J J, Senior T B A and Uslenghi P L E 1969 *Electromagnetic and Acoustic Scattering by Simple Shapes* (Amsterdam: North-Holland)
- [28] Polewski M and Mazur J 2002 Scattering by an array of conducting, lossy dielectric, ferrite and pseudochiral cylinders *Prog. Electromagn. Res.* **38** 283–310
- [29] Samaddar S N 1962 Scattering of plane waves from an infinitely long cylinder of anisotropic materials at oblique incidence with an application to an electronic scanning antenna *Appl. Sci. Res.* **10** 385–411
- [30] Seker S S and Schneider A 1988 Electromagnetic scattering from a dielectric cylinder of finite length *IEEE Trans. Antennas Propag.* **36** 303–7
- [31] Yang J, Li L-W, Yasumoto K and Liang C-H 2005 Two-dimensional scattering of a Gaussian beam by a periodic array of circular cylinders *IEEE Trans. Geosci. Remote Sens.* **43** 280–5
- [32] Yasumoto K and Jia H 2006 Modeling of photonic crystals by multilayered periodic arrays of Circular Cylinders *Electromagnetic Theory and Applications for Photonic Crystals* ed K Yasumoto (London: Taylor & Francis Group, LLC) p 123
- [33] Waterman P C 1971 Symmetry, unitarity and geometry in electromagnetic scattering *Phys. Rev. D* **3** 825–39
- [34] Sacher W D, Barwicz T, Taylor B J F and Poon J K S 2014 Polarization rotator-splitters in standard active silicon photonics platforms *Opt. Express* **22** 3777–86